Investigation of an isothermal Mach 0.75 jet and its radiated sound using large-eddy simulation and Kirchhoff surface integration

Niklas Andersson [a,*], Lars-Erik Eriksson [a,b], Lars Davidson [a]

[a] *Division of Thermo and Fluid Dynamics, Chalmers University of Technology, SE-412 96 Göteborg, Sweden*
[b] *Volvo Aero Corporation, Engines Division, SE-461 81 Trollhättan, Sweden*

Abstract

A large-eddy simulation (LES) of a compressible nozzle/jet configuration has been carried out. An isothermal Mach 0.75 jet was simulated. The Reynolds number based on the jet velocity at the nozzle exit plane and the nozzle diameter was 5.0×10^4. The Favre filtered Navier–Stokes equations were solved using a finite volume method solver with a low-dissipation third-order upwind scheme for the convective fluxes, a second-order centered difference approach for the viscous fluxes and a three-stage second-order Runge–Kutta time marching technique. A compressible form of Smagorinsky's subgrid scale model was used for computation of the subgrid scale stresses. The computational domain was discretized using a block structured boundary fitted mesh with approximately 3.0×10^6 cells. The calculations were performed on a parallel computer, using message-passing interface (MPI). Absorbing boundary conditions based on characteristic variables were adopted for all free boundaries. Velocity components specified at the entrainment boundaries were estimated from a corresponding Reynolds averaged Navier–Stokes (RANS) calculation, which enabled the use of a rather narrow domain. In order to diminish disturbances caused by the outlet boundary, a buffer layer was added at the domain outlet. Kirchhoff surface integration using instantaneous pressure data from the LES was utilized to obtain far-field sound pressure levels in a number of observer locations. The predicted sound pressure levels were for all observer locations within a 3 dB deviation from the measured levels and for most observer locations within a 1 dB deviation. Aerodynamic results and predicted sound pressure levels are both in good agreement with experiments. Experimental data were provided by Laboratoire d'Etude Aeró-dynamiques, Poitiers, France [Jordan, P., Gervais, Y., Valiére, J.-C., Foulon, H., 2002. Final results from single point measurements. Project deliverable D3.4, JEAN—EU 5th Framework Programme, G4RD-CT2000-00313, Laboratoire d'Etude Aeró dynamiques, Poitiers; Jordan, P., Gervais, Y., Valiére, J.-C., Foulon, H., 2002. Results from acoustic field measurements. Project deliverable D3.6, JEAN—EU 5th Framework Programme, G4RD-CT2000-00313, Laboratoire d'Etude Aeródynamiques, Poitiers; Jordan, P., Gervais, Y., 2003. Modeling self and shear noise mechanisms in anisotropic turbulence. In: The 9th AIAA/CEAS Aeroacoustics Conference. No. 8743 in AIAA 2003. Hilton Head, SC].

1. Introduction

Restrictions of noise levels in the surroundings of airports have made the reduction of near ground operation noise an important issue for aircraft and engine manufacturers, and noise generation has now become an important design factor taken into consid- eration early in the construction process. At take-off the main sources of noise are the propelling jet and the engine fan, of which the jet is usually the stron- gest noise source at full power. An EU project, JEAN (Jet Exhaust Aerodynamics and Noise), that focuses on investigating jet noise both numerically and exper- imentally and has a long term aim to improve exist- ing noise predicting tools, was started in February 2001. The work to be presented has been done within this project.

---
* Corresponding author. Tel.: +46 31 772 3788; fax: +46 31 180 976.
E-mail address: nian@tfd.chalmers.se (N. Andersson).

Nomenclature

c	speed of sound
C_p	specific heat at constant pressure
C_R, C_I	Smagorinsky model coefficients
D_j	nozzle outlet diameter
e	energy
f	frequency
k	kinetic energy
$\mathscr{L}$	integral length scale
L_c	potential core length
p	pressure
Pr	Prandtl number
Q	state vector
q_j	energy diffusion vector
$\mathscr{R}$	correlation amplitude
r	radial coordinate or distance from source to observer
Re_D	Reynolds number based on the jet diameter
S_{ij}	strain rate tensor
$\mathscr{T}$	integral time scale
T	temperature
t	time
(u, v, w)	axial, radial and tangential velocity component
u_i	Cartesian components of velocity vector
$\mathbf{x}$	flow field location
x_i	Cartesian coordinate vector component
$\mathbf{y}$	observer location

Greeks

Δ	filter width
δ_{ij}	Kronecker delta

μ	dynamic viscosity
ρ	density
σ_{ij}	viscous stress tensor
τ	temporal separation
τ_{ij}	subgrid scale stress tensor
τ_r	retarded time
θ	angle from the x-axis
ξ	spatial separation

Subscripts

0	total condition
∞	free stream or ambient conditions
c	center line
j	jet, nozzle exit condition
rms	root-mean-square
t	turbulent quantity

Superscripts

–	spatially filtered quantity
$'$	resolved fluctuation
$''$	unresolved quantity
$\sim$	spatially Favre filtered quantity
c	convection
exp	experiments
SGS	subgrid scale

Symbols

$\langle \cdots \rangle_\theta$	circumferentially averaged quantity
$\langle \cdots \rangle_t$	time-averaged quantity

Numerical methods based on computational fluid dynamics (CFD) used for prediction of flow-induced sound are often referred to as computational aeroacoustics (CAA). Using a grid fine enough in the far-field regions to minimize the introduction of sound propagation errors, the acoustic field can be obtained directly from the flow field simulation. This requires a detailed numerical compressible flow simulation, e.g. direct numerical simulation (DNS), see for example Freund (2001) and Mitchell et al. (1999), or large-eddy simulation (LES), as done by for example Bogey et al. (2000a) and Mankbadi et al. (2000).

To save computational time, a hybrid approach may be used in which the computational problem is divided into two parts. An LES or DNS can be used to obtain the non-linear near-field, which in the jet noise case corresponds to the hydrodynamic jet region. The acoustic field is then extended to far-field observer locations using either a solver based on the linearized Euler equations (LEE), see Billson et al. (2002), or an integral method such as Lighthill's acoustic analogy, as done by Bogey et al. (2001), or Kirchhoff surface integration, see Freund et al. (1996). In DNS, all scales of the turbulent flow field are computed accurately, which requires a mesh fine enough to capture even the smallest scales in the flow, whereas in LES, only the large scales of the flow are resolved and the influence on these large scales of the smaller, unresolved scales is modeled using a subgrid scale model. With the computational resources available today, DNS is restricted to fairly simple geometries and low Reynolds number flows. Moreover, it is believed, see Mankbadi (1999), that large scales are more efficient than small ones in generating sound, which justifies the use of LES for sound predictions.

Another approach is to use a less computationally expensive RANS calculation to obtain a time-averaged flow field. Information about length and time scales in the time-averaged flow field can then be used to synthe-

size turbulence in the noise source regions, see Billson (2004). This method is promising since simulations of high Reynolds number flows are possible with reasonable computational efforts. In contrast to a RANS calculation, where all turbulent scales in the flow are modeled and only a time-averaged flow field is obtained, DNS and LES directly provide information about turbulent quantities and sources of noise. To be able to improve existing CFD routines for more reliable results, we need an understanding of noise source mechanisms. Therefore, it is of great importance to perform more detailed calculations, such as DNS or LES, to get a more realistic picture of the flow physics. This is the main objective of the present work.

LES and DNS have been used for jet flow applications in a number of publications. These mostly study jets at moderate Reynolds number due to the high computational costs of performing simulations of a high Reynolds number jet. Many of these studies have been carried out in order to predict jet noise. However, as it is a free shear flow frequently occurring in both nature and industrial applications, the jet is interesting to study in itself. Some studies are thus pure investigations of flow phenomena.

The feasibility of using LES for both the flow field and the radiated sound from a high subsonic 6.5×10^4 Reynolds number jet has been discussed by Bogey et al. (2000a, 2001, 2003). In Bogey et al. (2000a, 2003), the acoustic field was obtained directly from the flow simulation. Noise generation mechanisms were found to be relatively independent of Reynolds number. In Bogey et al. (2001) Lighthill's acoustic analogy was used in combination with compressible LES to obtain the acoustic field. Bogey and Bailly (2003) investigated the effects of inflow conditions on the flow field and the radiated sound of a high Reynolds number, $Re_D = 4.0 \times 10^5$, Mach 0.9 jet. Both the flow development and the emitted sound were shown to depend appreciably on initial parameters. The effects of inflow conditions on the self-similar region were studied by Boersma et al. (1998) using DNS. The Reynolds number in this study was 2.4×10^3. Freund (2001) investigated sources of sound in a Mach 0.9 jet at a Reynolds number of $Re_D = 3.6 \times 10^3$ using DNS. In this work the part of the Lighthill source that may radiate to the far-field was isolated using Fourier methods. It was found that the peak of the radiating source coincides with neither the peak of the total source nor the peak of turbulence kinetic energy. The flow field and the radiated sound of a supersonic low Reynolds number jet (Mach 1.92, $Re_D = 2.0 \times 10^3$) was predicted using DNS by Freund et al. (2000). DeBonis and Scott (2002) used LES to obtain the flow field of a supersonic high Reynolds number jet (Mach 1.4, $Re_D = 1.2 \times 10^6$) from which two-point space-time correlations in the jet shear-layer were obtained. Turbulence scales obtained from the correlations were found to be in good agreement with theory. In this study the nozzle geometry was included in the calculation domain. Shur et al. (2003) made simulations of a cold Mach 0.9 jet at a Reynolds number of 1.0×10^4. Radiated sound was successfully predicted using Ffowcs Williams and Hawkings (1969) surface integral formulation, which since the surface is stationary becomes identical to the formulation by Curle (1955). The simulation was conducted using only 5.0×10^5 cells. This work was done using the monotone-integrated LES (MILES) approach where the subgrid scale model is replaced by the numerical dissipation of the numerical method used. Tucker (2004) investigated the effects of co-flow and swirl on the flow in the initial jet region and the radiated noise of a high subsonic jet (Mach 0.9, $Re_D = 1.0 \times 10^4$) using a hybrid RANS/MILES approach. Le Ribault et al. (1999) performed large-eddy simulations of a plane jet at two Reynolds numbers, $Re = 3.0 \times 10^3$ and $Re = 3.0 \times 10^4$. Simulations were performed for both Reynolds numbers using different subgrid scale models to investigate the ability of the models to capture the jet flow physics. Zhao et al. (2001) conducted an LES of a Mach 0.9 jet at Reynolds number 3.6×10^3 and a jet at Mach 0.4 and a Reynolds number of 5.0×10^3. In this study, radiated sound was obtained both directly from the LES and by using Kirchhoff surface integration. The effect on the radiated sound of the subgrid scale model was investigated. It was found that using a mixed subgrid-scale model resulted in both higher turbulence levels and sound levels. Rembold et al. (2002) investigated the flow field of a rectangular jet at Mach 0.5 and a Reynolds number of 5.0×10^3 using DNS.

In the present study an LES of a Mach 0.75 nozzle/jet configuration has been performed (see Table 1). The Reynolds number based on the nozzle exit diameter and the jet velocity at the nozzle exit plane, Re_D, was 5.0×10^4. The Reynolds number in the measurements (Jordan et al., 2002a,b; Jordan and Gervais, 2003; Power et al., 2004), used for comparison and validation of the simulations, was approximately one million. Such a high Reynolds number probably means that the scales that need to be resolved are too small. Thus the

Table 1
Flow properties

U_j/c_∞	T_j/T_∞	P_∞ (Pa)	ρ_∞ (kg m^{-3})	c_∞ (m s^{-1})	U_∞ (m s^{-1})	T_∞ (K)	T_{0_j} (K)	Re_D[a]
0.75	1.0	101300	1.22556	340.174	0.0	288.0	320.4	5.0×10^4

[a] The Reynolds number was decreased using modified viscosity.

Reynolds number in our LES was decreased with the assumption that the flow is only weakly Reynolds number dependent. A nozzle geometry is included in the calculation domain corresponding to the last contraction of the nozzle configuration in the experimental setup used for the measurements by Jordan et al. An isothermal jet is simulated, i.e. the static temperature in the nozzle exit plane, T_j, is equal to the static temperature of the ambient air, T_∞. For validation of the LES results, the time-averaged flow is compared with experimental data provided by Laboratoire d'Etude Aeródynamiques, Poitiers, France (Jordan et al., 2002a).

Two-point space-time correlations are obtained for a few locations in the shear-layer, and integral length and time scales and eddy convection velocities are evaluated. Two-point measurements in the shear-layer at $x = L_c$ and $x = 0.75L_c$ done by Jordan and Gervais (2003) are used for comparison.

Evaluation is made of far-field sound pressure levels using Kirchhoff surface integration. Predicted sound pressure levels are compared with experimental results (Jordan et al., 2002b).

2. Governing equations

The equations solved are the spatially Favre filtered continuity, momentum and energy equations,

$$\frac{\partial \bar{\rho}}{\partial t} + \frac{\partial (\bar{\rho}\tilde{u}_i)}{\partial x_i} = 0, \tag{1}$$

$$\frac{\partial (\bar{\rho}\tilde{u}_i)}{\partial t} + \frac{\partial (\bar{\rho}\tilde{u}_i\tilde{u}_j)}{\partial x_j} = -\frac{\partial \bar{p}}{\partial x_i} + \frac{\partial \bar{\sigma}_{ij}}{\partial x_j} + \frac{\partial \tau_{ij}}{\partial x_j}, \tag{2}$$

$$\frac{\partial (\bar{p}\tilde{e}_0)}{\partial t} + \frac{\partial (\bar{p}\tilde{e}_0\tilde{u}_j)}{\partial x_j} = -\frac{\partial \bar{p}\tilde{u}_j}{\partial x_j} + \frac{\partial}{\partial x_j}\left(C_p\frac{\mu}{Pr}\frac{\partial \tilde{T}}{\partial x_j} + q_j\right)$$
$$+ \frac{\partial}{\partial x_j}(\tilde{u}_i(\bar{\sigma}_{ij} + \tau_{ij})), \tag{3}$$

where $\bar{\sigma}_{ij}$ and τ_{ij} are the Favre filtered viscous stress tensor and subgrid scale viscous stress tensor, respectively. These are here defined as

$$\bar{\sigma}_{ij} = \mu\left(2\tilde{S}_{ij} - \frac{2}{3}\tilde{S}_{mm}\delta_{ij}\right), \tag{4}$$

$$\tau_{ij} = \mu t\left(2\tilde{S}_{ij} - \frac{2}{3}\tilde{S}_{mm}\delta_{ij}\right) - \frac{2}{3}\bar{\rho}k^{\text{SGS}}\delta_{ij}, \tag{5}$$

where k^{SGS} is the subgrid scale kinetic energy

$$k^{\text{SGS}} = C_I\Delta^2\tilde{S}_{mn}\tilde{S}_{mn}, \tag{6}$$

μ_t the subgrid scale dynamic viscosity

$$\mu_t = C_R\bar{\rho}\Delta^2\left(\tilde{S}_{mn}\tilde{S}_{mn}\right)^{0.5}, \tag{7}$$

and $\tilde{S}_{ij}$ is the Favre filtered strain rate tensor given by,

$$\tilde{S}_{ij} = \frac{1}{2}\left(\frac{\partial \tilde{u}_i}{\partial x_j} + \frac{\partial \tilde{u}_j}{\partial x_i}\right) \tag{8}$$

The subgrid heat flux appearing in the Favre-filtered energy equation is modeled using a temperature gradient approach

$$q_j = C_p\frac{\mu_t}{Pr_t}\frac{\partial \tilde{T}}{\partial x_j}. \tag{9}$$

The filter-width used in Eqs. (6) and (7) is the local grid cell width, i.e. $\Delta = (\Delta_1\Delta_2\Delta_3)^{1/3}$. The subgrid scale model used in this work is the Smagorinsky part of the model proposed by Erlebacher et al. (1992) for compressible flows. The Smagorinsky model constants C_R and C_I were proposed by Erlebacher et al. (1992) to be

$$\begin{cases} C_R = 0.12, \\ C_I = 0.66. \end{cases} \tag{10}$$

The system of governing equations, Eqs. (1)–(3), is closed by making assumptions concerning the thermodynamics of the gas considered. It is assumed that the gas is thermally perfect, i.e. it obeys the gas law. Furthermore, the gas is assumed to be calorically perfect, which implies that internal energy and enthalpy are linear functions of temperature.

3. Kirchhoff surface integral formulation

Kirchhoff integration is a method for predicting the value of a property, Φ, governed by the wave equation, at a point outside a surface enclosing all generating structures (Lyrintzis, 1994).

$$\Phi(\mathbf{y}, t) = \frac{1}{4\pi}\int_s \left[\frac{\Phi}{r^2}\frac{\partial r}{\partial n} - \frac{1}{r}\frac{\partial \Phi}{\partial n} + \frac{1}{c_\infty r}\frac{\partial r}{\partial n}\frac{\partial \Phi}{\partial t}\right]_{\tau_r} \mathrm{d}S(\mathbf{x}), \tag{11}$$

where τ_r denotes that the expression within brackets is to be evaluated at retarded time, i.e. emission time. τ_r is related to the observer evaluation time, t, as

$$\tau_r = t - \frac{r}{c_\infty}, \tag{12}$$

where r is the distance between a point on the surface, $\mathbf{x}$, and an observer location, $\mathbf{y}$. c_∞ is the speed of sound in the far-field region. The variable, Φ, to be evaluated, is in this case the surface pressure. S denotes the surface enclosing all sound generating structures and n denotes the direction normal to the surface. The surface, S, must be placed in a region where the flow is completely governed by a homogeneous linear wave equation with constant coefficients (Freund et al., 1996). More detail on the Kirchhoff surface integration method, can be found in e.g. Freund et al. (1996) and Lyrintzis (1994).
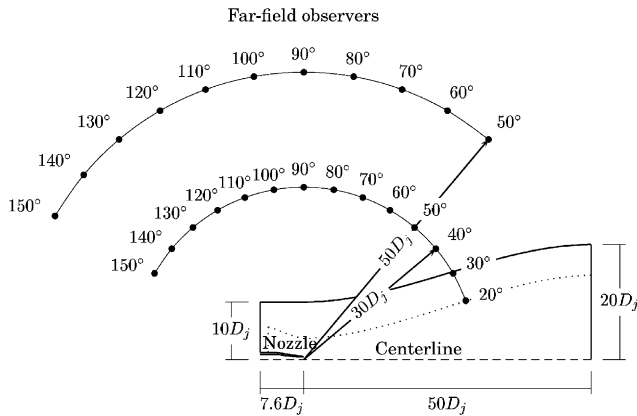
Fig. 1. Kirchoff surface (dotted line) and far-field observer locations.

The strength of the sources in the hydrodynamic jet region decays slowly downstream, which means that the downstream end of a closed surface will enter regions of considerable hydrodynamic fluctuations. It is thus common practice to use Kirchhoff surfaces not closed in the upstream and downstream ends. It has been shown by Freund et al. (1996) that the errors introduced by using such surfaces are small if the main portion of the sound sources are within the axial extent of the surface and if lines connecting observer locations with locations in the hydrodynamic region, representing the main sources of sound, intersect with the surface.

In this work a Kirchhoff surface closed in the upstream end and open in the downstream end was used, see Fig. 1.

4. Numerical method

4.1. Numerical scheme

The governing equations were solved using a cell centered finite volume method solver. A low-dissipation third-order upwind scheme was used for discretization of the convective fluxes and a second-order central difference approach for the viscous fluxes. The convective scheme is a combination of centered and upwind biased components that have been used with good results for free shear flows by Mårtensson et al. (1991) and, more recently, for shock/shear-layer interaction by Wollblad et al. (2004). Appendix A gives more detail on the convective flux scheme.

Time marching is performed using a second-order three-stage Runge–Kutta technique. For more detail on the numerical scheme used, see Eriksson (1995) or Andersson (2003). The computations were performed in part on a Sun-cluster using 14 SunBlade 750 MHz processors and in part on a Linux cluster using 14 AMD 1700[+] processors. MPI (Message Passing Inter-

face) routines were implemented for processor communication.

4.2. Computational domain

The computational domain consists of a boundary-fitted block structured mesh with 50 blocks and a total of about 3.0×10^6 cells excluding the buffer region at the domain outlet, see Figs. 2–4. The grid cells are concentrated to the shear-layer area. To establish mesh homogeneity, a combination of polar and cartesian blocks was used, see Fig. 4. The grid cells are stretched in the downstream direction and radially toward the boundaries using cubic Hermite grid point distribution. The last contraction of the JEAN project nozzle
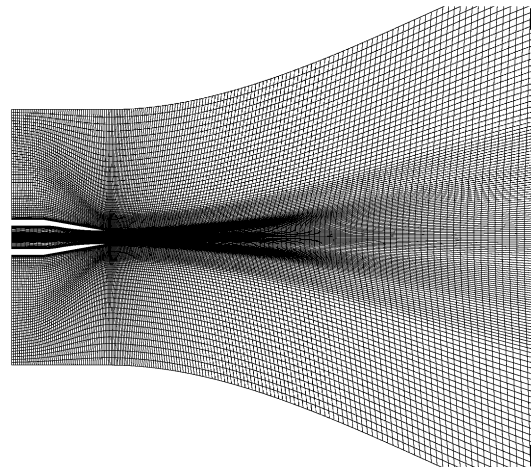
Fig. 2. A slice through the calculation domain made at $z = 0$, i.e. a xy-plane, is depicted. The figure shows the domain inlet including the nozzle and the outer boundaries in the radial direction. The axial extent of the computational domain is roughly twice that shown in the figure.
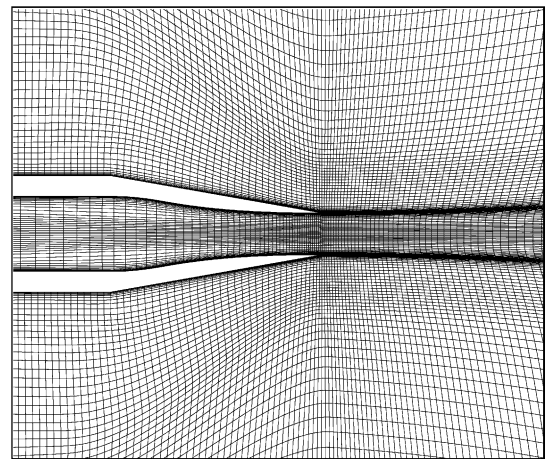
Fig. 3. A slice of the calculation domain in the nozzle region is shown. Cells are concentrated to the shear-layer area.
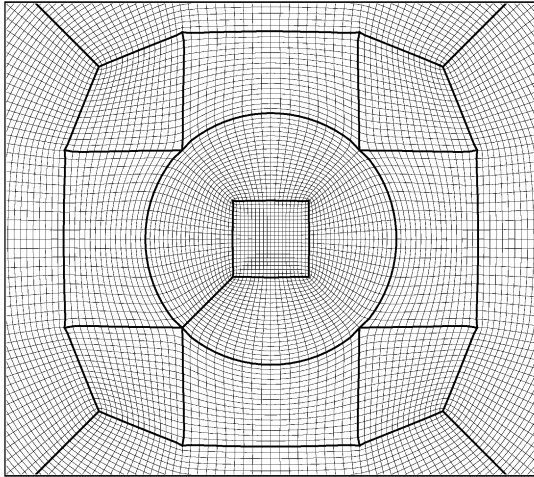
Fig. 4. A slice through the calculation domain at constant x, i.e. a yz-plane, is depicted. Combining Cartesian and polar grid blocks enhances the radial direction grid homogeneity throughout the domain.
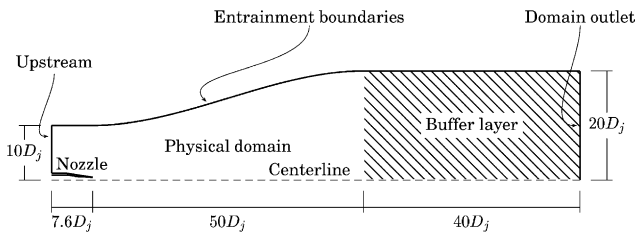
Fig. 5. Computational setup. $D_j = 50$ [mm].

is included in the calculation domain. The axial extent of the physical part of the domain is 2.5 m, which is equal to 50 nozzle diameters ($D_j = 50$ [mm]). The radial extent is 10 nozzle diameters at the nozzle exit plane and 20 diameters at the domain outlet, see Fig. 5.

4.3. Boundary conditions

At the inlet of the nozzle, the nozzle plenum, total pressure and total enthalpy are specified. All free boundaries, i.e. upstream and entrainment boundaries, are defined using absorbing boundary conditions based on characteristics variables. At the domain outlet static pressure is specified. In Fig. 5 the main boundary condition locations are depicted.

Defining proper boundary conditions is an issue of great importance, especially in aeroacoustic applications since acoustic pressure fluctuations are small and spurious waves generated at the boundaries might contaminate the acoustic field. Definitions of boundary conditions for free shear flows are particularly difficult since there are, by definition, no bounding surfaces. The difficulties in defining boundary conditions for free shear flows have been discussed in several publications

(e.g. Colonius et al., 1993; Mankbadi et al., 2000; Bogey et al., 2000b; Rembold et al., 2002).

At a finite distance downstream the jet, boundary conditions that mimic the jet behavior at infinity are to be specified. Energetic vorticity and entropy waves traveling out of the domain reaching the outlet boundary will, if not damped out, generate strong acoustic waves traveling back into the domain. These acoustic reflections can be diminished by in some way decreasing the amplitude of fluctuations of vorticity and entropy waves approaching the boundary. Inward traveling acoustic waves may still be generated but will be weaker than for a boundary where no special treatment of the boundary region is utilized. Moreover, these weaker acoustic waves are additionally damped when traveling through the outlet region on their way back into the calculation domain and, hopefully, the waves are so weak when reaching the jet region that they do not affect the results. In order to dampen acoustic reflections, an extra outlet zone has been added to the calculation domain, Fig. 5, where a damping term defined by

$$\varepsilon(Q - \langle Q \rangle) \tag{13}$$

has been added to the equation system, ε is defined by a constant, ε_{max} and the axial location, x, in the damping zone as

$$\varepsilon = \varepsilon_{max} \left(\frac{x - x_{min}}{x_{max} - x_{min}} \right)^2. \tag{14}$$

In Eq. (13), Q represents the flow variables and the time-average of Q is calculated as

$$\langle Q \rangle = \frac{\sum_{i=1}^{n} Q_i t_i}{\sum_{i=1}^{n} t_i}, \tag{15}$$

where subscript i denotes time step. The weighted time-average defined by Eq. (15) gives the recent flow property values higher weight than older values and it also gives a good estimate of the time-averaged flow field. The fluctuations of the flow field are damped in the boundary zone by forcing the flow properties toward the time-averaged flow field. Furthermore, the cells in this part of the calculation domain are more stretched than cells in the physical part of the calculation domain, which increases the numerical dissipation and thereby further damps flow field fluctuations. The boundary zone consists of roughly 5.0×10^5 cells, which is about 14% of the total calculation domain, and has an axial extent of 40 jet diameters, see Fig. 5.

The entrainment boundaries proved to be rather troublesome as well. The problem is to get enough fluid entrainment into the domain. The effect of not getting the entrained mass flow correct is that a deficit of mass is compensated with an inflow of fluid from the domain outlet. This back flow results in a recirculation zone surrounding the jet and prevents it from spreading.

Approximate values of the velocities specified at the entrainment boundaries were obtained from RANS calculations with $U_\infty = 0$ (Eriksson, 2002). These RANS calculations were performed using significantly larger calculation domain than in the LES and therefore give reliable information on the entrainment effect at the boundary of the LES domain. Furthermore, these RANS calculations have been extensively validated against experimental data (Jordan et al., 2002a). The fact that the boundary values at the entrainment boundaries have been obtained from RANS results does, to a certain degree, determine the time-averaged flow field. However, since this work is not an attempt to prove that large-eddy simulation predicts the flow of a jet properly but rather to obtain a database of flow properties for jets and to get input for calculations of the acoustic field, this is no severe disadvantage.

5. Results

Profiles of statistical quantities shown in Figs. 6–14 are obtained from flow field data that were averaged in both time and the azimuthal direction to establish
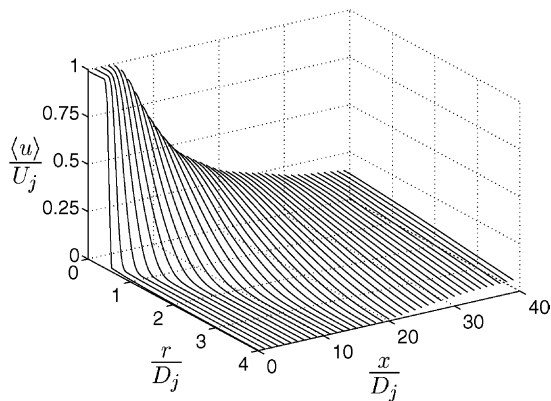
Fig. 6. Downstream development of radial profiles of axial velocity.
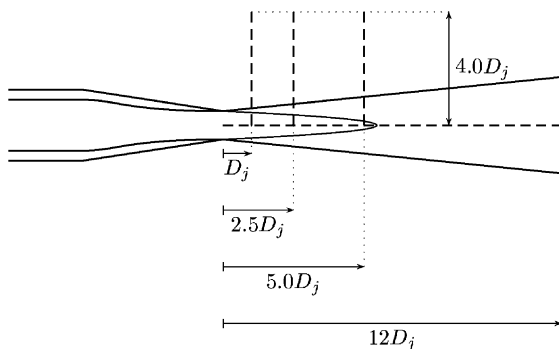
Fig. 7. Profiles of axial velocity and second-order moments were obtained along the centerline and along three radial lines.
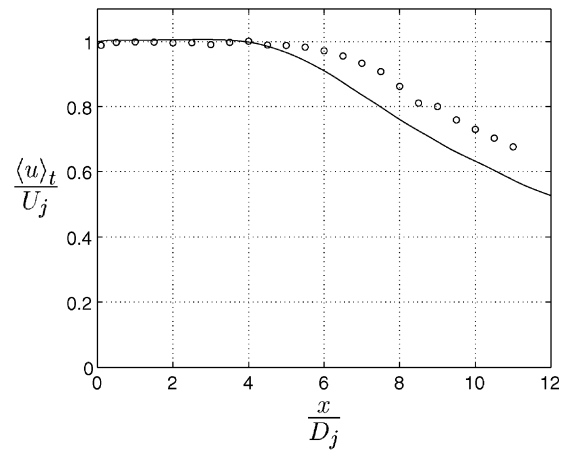
Fig. 8. Center line velocity: the solid line, '—', corresponds to LES results and the circles, '○', to experimental data (Jordan et al., 2002a).
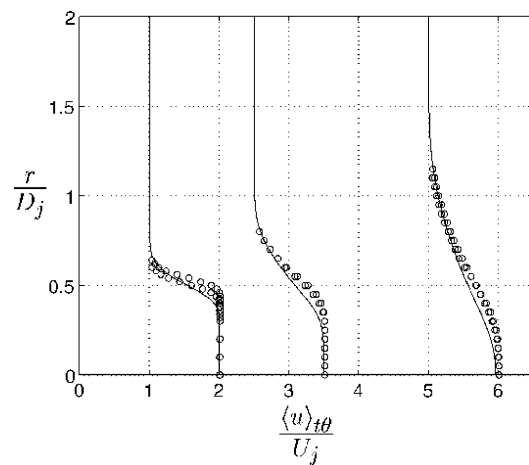
Fig. 9. Radial profiles of axial velocity at the axial positions $x/D_j = 1.0$, $x/D_j = 2.5$ and $x/D_j = 5.0$: '—' corresponds to LES results and '○' to experimental data (Jordan et al., 2002a). The profiles have been staggered corresponding to their axial position.
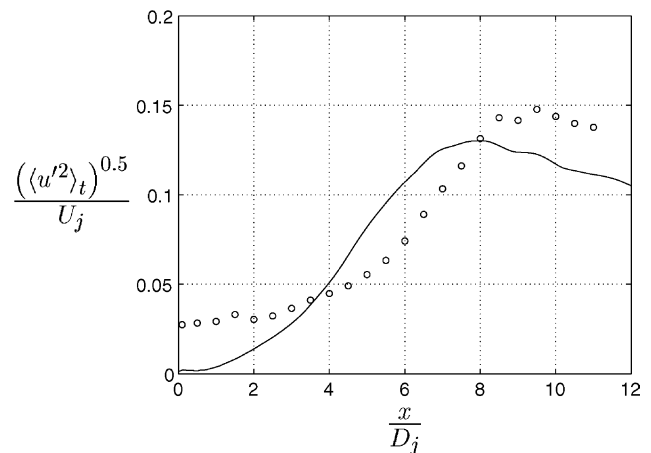
Fig. 10. Axial profile of $(\langle u'u'\rangle_t)^{0.5}$: '—' corresponds to LES results and '○' to experimental data (Jordan et al., 2002a).

Fig. 11. Radial profiles of $(\langle u'u'\rangle_{t\theta})^{0.5}$. See also legend to Fig. 9.
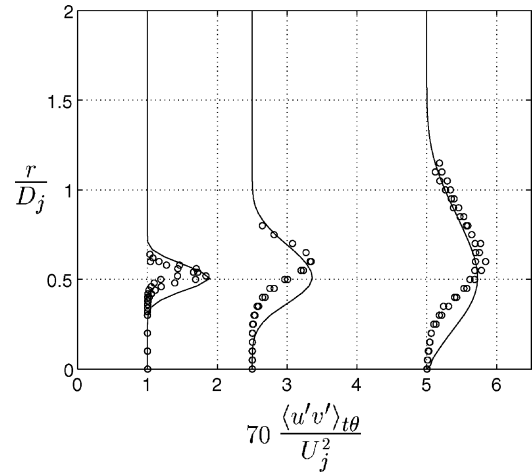
Fig. 14. Radial profiles of $(u'v')_{t\theta}$. See also legend to Fig. 9.
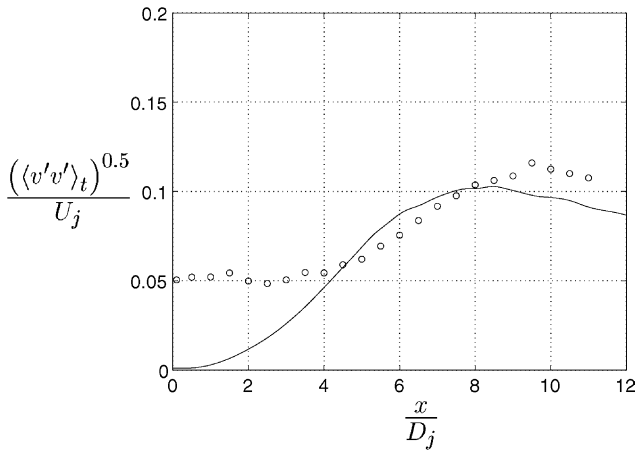
Fig. 12. Axial profile of $(\langle v'v'\rangle_t)^{0.5}$: '—' corresponds to LES results and 'O' to experimental data (Jordan et al., 2002a).
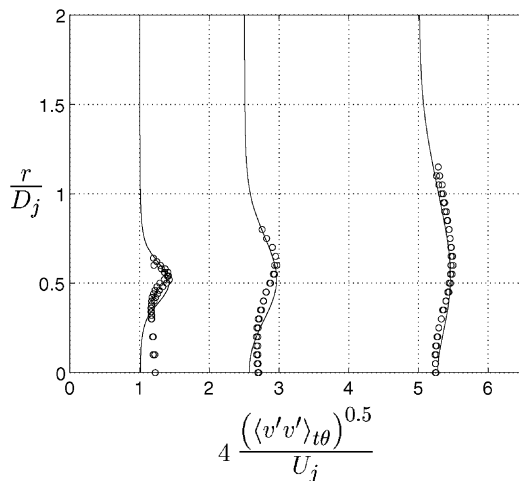
Fig. 13. Radial profiles of $(\langle v'v'\rangle_{t\theta})^{0.5}$. See also legend to Fig. 9.

improved statistical convergence. The profiles are made non-dimensional using the jet velocity at the nozzle exit, U_j, and the nozzle outlet diameter, D_j.

The calculations were started up using an initial solution interpolated from RANS. The simulation ran for about 1.0×10^5 time steps before sampling was initiated. This corresponds to 0.025 s of simulated time using a time step of 0.25 [μs] or roughly 3.5 acoustic through-flows, i.e. the time required for an acoustic wave to travel through the calculation domain, not including the outlet buffer layer, based on the speed of sound at ambient conditions. Sampling of statistic data was then continued for another 20 acoustic through-flows. Each acoustic through-flow corresponds to roughly 32 h of computer wall-time using 14 AMD 1700[+] processors of our Linux cluster. The time step is chosen such that the CFL (Courant–Friedrichs–Lewy) number was not larger than 0.5 any where.

5.1. Time-averaged profiles

Fig. 6 depicts the development of radial profiles of axial velocity downstream of the nozzle exit. Comparison of profiles obtained from LES and experiments are presented in Figs. 8–14. The radial profiles have been staggered corresponding to the axial position, i.e. 1.0, 2.5 and 5.0 jet diameters respectively, to show downstream development. Furthermore, it should be noted that, in order to obtain similar scales for all the radial profile figures, root-mean-square values and $u'v'$ correlations have been multiplied by a factor 4 and 70, respectively. The location of the lines along which axial and radial profiles have been extracted is shown in Fig. 7.

Although the LES results are generally in good agreement with experiments, there are some deviations. The main discrepancy is that the LES fails to predict the length of the jet potential core, see Fig. 8, and thereby the location of maximum turbulence intensity, see Figs.

10 and 12. It has been mentioned by DeBonis and Scott (2002) that this is generally not the case in earlier studies of jets; rather, the length of the potential core is usually overpredicted. Although the location of the potential core closure is not accurately predicted, the rate of decay of the centerline axial velocity is.

Centerline profiles of u'_{rms} and v'_{rms} are shown in Figs. 10 and 12, respectively. The maximum level is in both cases somewhat underpredicted but, as can be seen by comparing the two figures, the turbulence anisotropy of the jet has been correctly predicted. Significant deviations from experimental data in root-mean-square values of radial velocity near the centerline, Figs. 12 and 13, might be due to low frequency flutter of the potential core found in the experiments (Jordan et al., 2002a) but not present in the computations. Compared to the measured profiles, the peaks of the predicted u'_{rms} are shifted toward the centerline for the radial profiles at $x/D_j = 1.0$ and $x/D_j = 2.5$, see Fig. 11. This is consistent with the shift of the radial profiles of axial velocity, i.e. the maximum turbulence intensity should appear at a radial location close to the maximum radial derivative of the axial velocity. However, the peak levels of u'_{rms} are very close to those of the measured profiles, which is surprising since the radial gradients is smaller for the predicted axial velocity. The overpredicted $u'v'$ correlation, see Fig. 14, is an indication of the turbulent mixing being too high and thus totally in line with the shorter potential core. For a more correct comparison, the subgrid scale component of the shear stress, $\widetilde{u''v''}$, should be added to the resolved, $u'v'$. However, as can be seen in Fig. 15 where the sub-grid scale shear stress is compared with the resolved shear stress, the subgrid scale component is as most roughly 4.0% of the resolved and can thus be neglected.

The reason for the underprediction of the length of the potential core region can probably be found in a combination of several factors. The most important are probably subgrid scale viscosity, numerical scheme, entrainment boundary conditions and inflow conditions. DeBonis and Scott (2002) reported an underprediction of the potential core region when using LES for a supersonic jet. It was discussed in this work that the reason for this underprediction was lack of subgrid dissipation. Furthermore, it has been mentioned by Morris et al. (2000) that a change in the subgrid scale model constants affects the potential core length and the initial growth of the jet. DeBonis (2004) found that the potential core region could be extended by increasing the subgrid scale dissipation. This is a quite natural effect since the increased subgrid scale viscosity decreases the turbulent fluctuations and hence the shear-layer mixing becomes less effective. This in turn leads to an elongated region of potential flow. Figs. 16 and 17 depicts subgrid scale viscosity over molecular viscosity and subgrid scale kinetic energy over resolved turbulent kinetic energy, respectively. The profiles of subgrid scale viscosity indicate that the LES is of good quality. From Fig. 17 it can be seen that the subgrid scale kinetic energy is as most about 1.0% of the resolved. Lack of subgrid scale dissipation might be a reason for the underpredicted potential core seen in the present study. It is, however, not obvious that this is the only reason for this shorter potential core; rather it might be one of several factors. Tucker (2004) used a scheme for the convective fluxes based on a weighted average of centered and upwind biased components. It was found that even with a weak blending of fifth order upwinding with a fourth order central scheme, i.e. only small contributions from the upwind biased components, the effects of the upwind scheme is still evident. However, the effect of the artificial
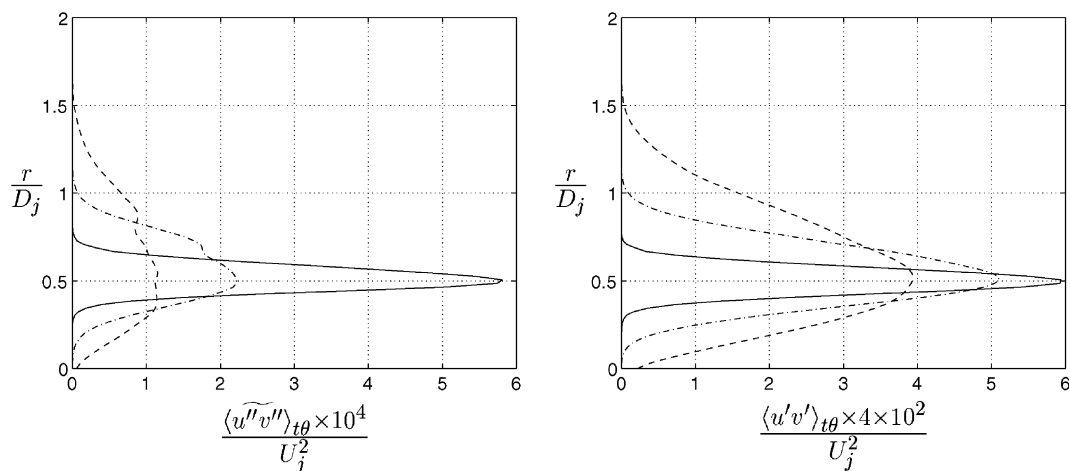

Fig. 15. Radial profiles of subgrid scale (left) and resolved (right) $u'v'$ correlations. It should be noted that the values in the left figure have been multiplied by a factor 10^4 and those in the right figure by a factor 4×10^2: the solid line denotes $x/D_j = 1.0$, dash-dotted line $x/D_j = 2.5$ and dashed line $x/D_j = 5.0$.
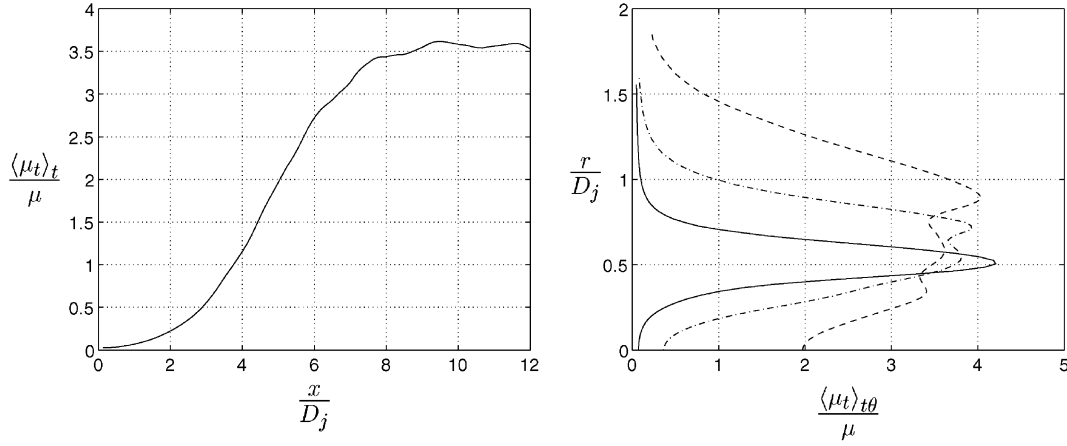
Fig. 16. Axial (left) and radial (right) profiles of subgrid scale viscosity over molecular viscosity. In the right figure, the solid line denotes $x/D_j = 1.0$, dash-dotted line $x/D_j = 2.5$ and dashed line $x/D_j = 5.0$.
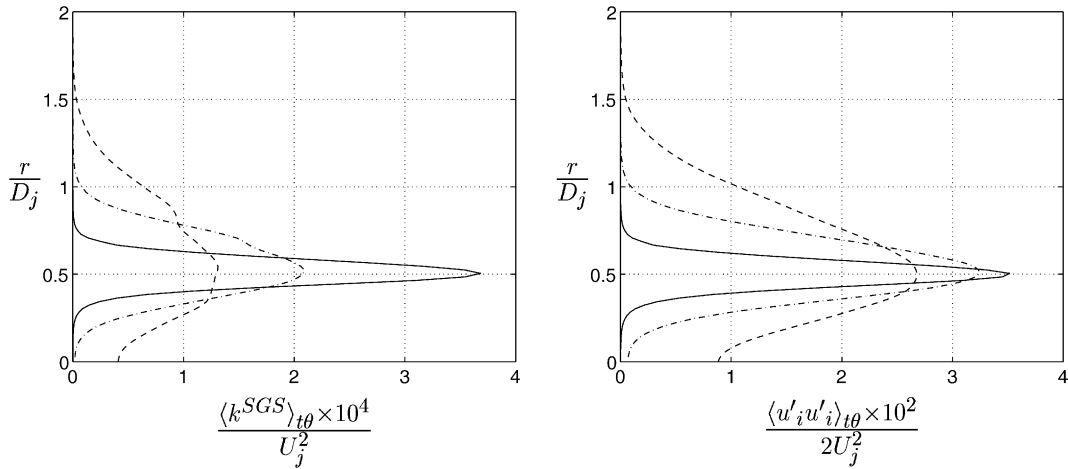

Fig. 17. Radial profiles of subgrid scale (left) and resolved (right) turbulence kinetic energy. Note that to be able to compare the profiles, the subgrid values have been multiplied by a factor 10^4 and the resolved values by a factor 10^2. See also legend to Fig. 16.

dissipation introduced by the numerical scheme used ought to be the same as that of the subgrid scale dissipation, i.e. more numerical dissipation leads to a longer potential core due to less efficient turbulent mixing. Consequently, the numerical scheme used for the present work does not introduce too much artificial dissipation since the turbulent mixing is overpredicted. Concerning the effects of the entrainment flow, only the correct mass flow will give the correct flow behavior in the hydrodynamic region. As discussed in Section 4.3, lack of entrained mass will be compensated by back flow, which results in a recirculation zone surrounding the jet and prevent it from spreading correctly. However, the RANS computations from which the boundary entrainment velocities have been interpolated, gives a somewhat overpredicted potential core length. Other effects that may well be important are the velocity profile and turbulence level at the nozzle exit. Having a velocity profile at the nozzle exit that is not fully developed re-

sults in steep velocity gradients and therefore a more violent encounter with the irotational surrounding fluid. This may result in larger fluctuations and thus also higher degree of turbulent mixing. Bogey and Bailly (2003) investigated the effects of the inflow conditions on the jet flow. It was found that the use of a thinner shear-layer momentum thickness resulted in higher turbulence intensities in the shear-layer and hence a more rapid transition. In summary, the correct potential core length may be obtained by modification of the subgrid scale properties alone. However, a more physical approach would be to modify the inflow conditions to produce results in better agreement with measurements.

5.2. Self-preservation

Radial profiles of axial velocity and second-order moments were normalized by centerline velocity and plotted versus a non-dimensional radial coordinate to

investigate whether or not self-preservation has been established. These profiles were obtained using statistical flow field data averaged in time and the azimuthal direction. The constant, x_0, used to collapse the profiles is a virtual origin obtained from the least square fit of data points in Fig. 18, i.e. the axial position for which $U_j/\langle u_c \rangle_t = 0$. In this case $x_0 = 0.11D_j$. As seen in Fig. 18, a non-negligible deviation from the linear relation occurs for centerline points located between $20D_j$ and $35D_j$, downstream of the nozzle exit. This behavior is probably due to the entrainment boundary conditions used. However, since this occurs far downstream, the effect on the flow field in the region near the nozzle exit ($x < 20D_j$) is probably negligible. Fig. 19 shows collapsed radial profiles of axial velocity. Five radial profiles equally spaced between $19D_j$ and $39D_j$ were used. The jet spreading rate can be estimated to be roughly

0.09 based on the curve fitted to the LES data. Figs. 20–23 depict normalized profiles of second-order moments. For these figures, radial profiles in six axial positions from $29D_j$ to $39D_j$ downstream of the nozzle were used. The distance between each profile is, in this case, two jet diameters. As can be seen in the Figs. 19–23, self-preservation of axial velocity has been well established within 39 jet diameters downstream of the nozzle whereas, for self-preservation of second-order moments to be obtained data would have to be extracted further downstream. For example Hussein et al. (1994) found that profiles of second and higher order moments displayed self-similar behavior when evaluated at axial positions more than $70D_j$ downstream of the virtual

Fig. 18. Predicted center line velocity. The solid line corresponds to a curve fit to the LES data. The x-value for which the line intersects the x-axis, x_0, is used to collapse the radial profiles in Figs. 19–23.
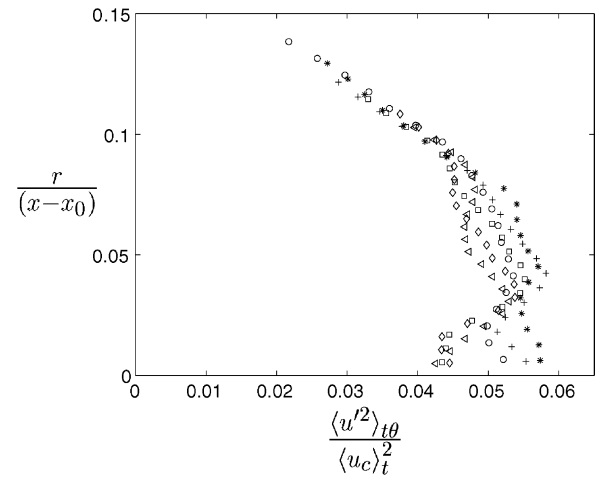

Fig. 20. Radial profiles of $\langle u'u' \rangle_{t\theta}$ normalized by centerline mean velocity. Radial profiles at six axial locations are represented. The profiles are labeled as follows: '$\bigcirc$' = $29D_j$, '$\ast$' = $31D_j$, '+' = $33D_j$, '$\square$' = $35D_j$, '$\diamond$' = $37D_j$ and finally '$\triangleleft$' = $39D_j$.

Fig. 19. Radial profiles of axial velocity normalized by centerline mean velocity. The solid line corresponds to a curve fit to the LES data. The profiles are labeled as follows: '$\bigcirc$' = $19D_j$, '$\ast$' = $24D_j$, '+' = $29D_j$, '$\square$' = $34D_j$ and '$\diamond$' = $39D_j$.
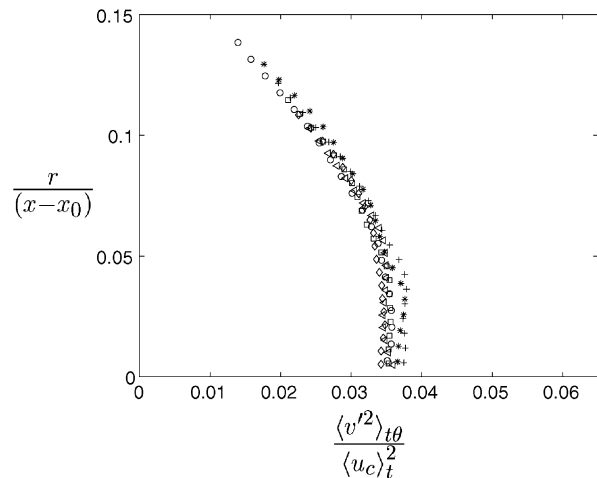

Fig. 21. Radial profiles of $\langle u'v' \rangle_{t\theta}$ normalized by centerline mean velocity. For legend see Fig. 20.
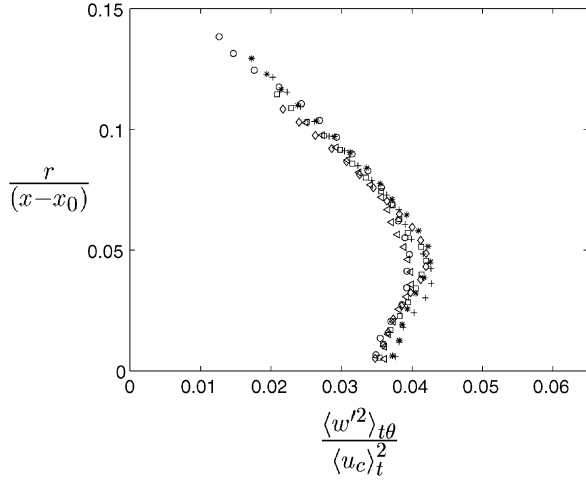
Fig. 22. Radial profiles of $\langle w'w'\rangle_{t\theta}$ normalized by centerline mean velocity. For legend see Fig. 20.
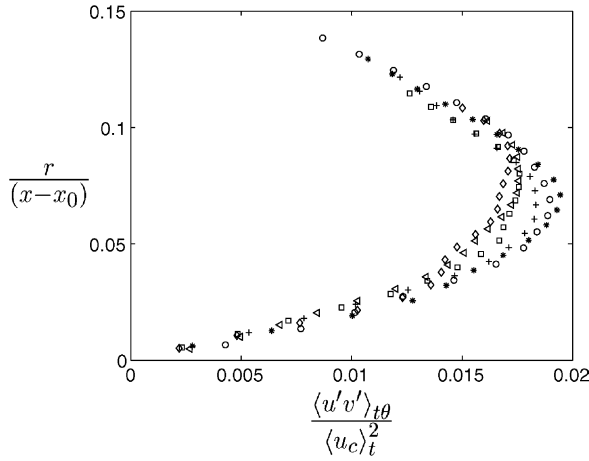

Fig. 23. Radial profiles of $\langle u'v'\rangle_{t\theta}$ normalized by centerline mean velocity. For legend see Fig. 20.

origin. However, this would require a larger computational domain to be used.

5.3. Two-point space-time correlations

Two-point space-time correlations were obtained for axial velocity in a few points in the shear-layer region downstream of the nozzle exit. The time series used is 0.0725 s. Spatial separations, ξ, are in this case downstream in the axial direction. The two-point space-time correlation of axial velocity for a certain spatial separation, ξ, and separation in time, τ, is given by

$$\mathscr{R}_{uu}(\mathbf{x},\xi,\tau) = \frac{\langle u'(\mathbf{x},t)u'(\mathbf{x}+\xi,t+\tau)\rangle_t}{(\langle u'^2(\mathbf{x})\rangle_t)^{0.5}(\langle u'^2(\mathbf{x}+\xi)\rangle_t)^{0.5}}, \qquad (16)$$

where u' denotes fluctuation of axial velocity and $\mathbf{x}$ is the position in the flow field where the two-point correlation is evaluated, see Fig. 24. Figs. 25–27 show two-point

Fig. 24. Two-point space-time correlations in the shear-layer are obtained for location, $\mathbf{x}$, using a spatial separation, ξ.
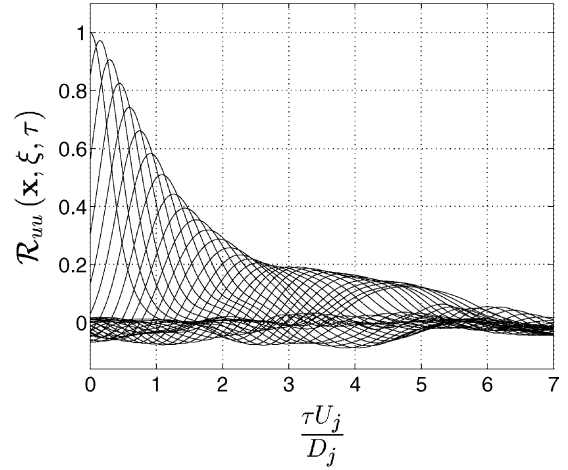
Fig. 25. Two-point space-time correlation of axial velocity in the shear-layer at $r = 0.5D_j$, $x = 2.5D_j$. Each curve corresponds to a two-point space-time correlation obtained using a certain spatial separation, ξ. Starting with no separation in space, i.e. the autocorrelation, the spatial separation is increased by $0.1D_j$ per curve.
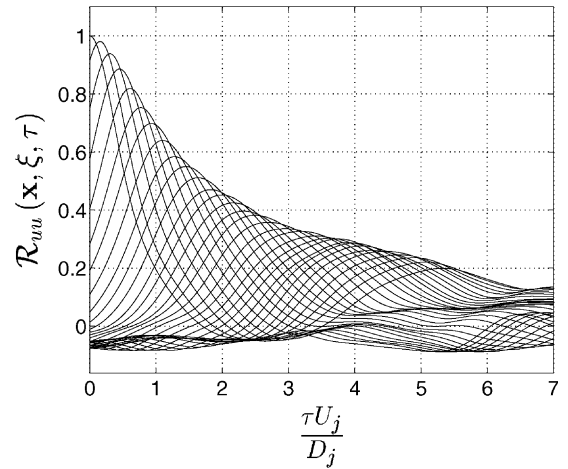

Fig. 26. Two-point space-time correlation of axial velocity in the shear-layer at $r = 0.5D_j$, $x = 5.0D_j$. See also legend to Fig. 25.

correlations in points located on the nozzle lip-line 2.5, 5.0 and 10.0 nozzle diameters downstream of the nozzle exit. Each figure includes the autocorrelation of axial velocity fluctuations, i.e. no spatial separation, and 30 two-point space-time correlations obtained with increased spatial separation. Each consecutive correlation curve corresponds to an increase in spatial separation by $0.1D_j$. The integral of the envelope built up of the two-point space-time correlation curves corresponds to a
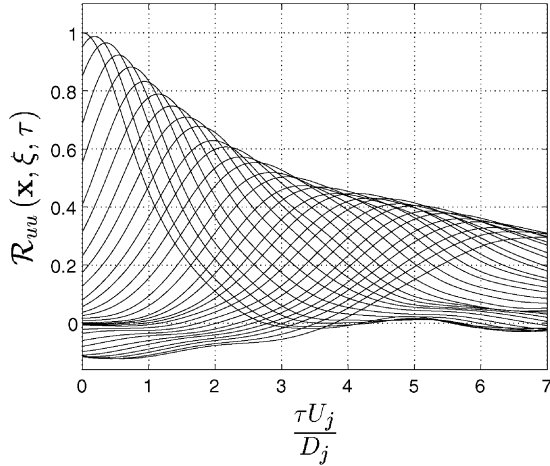
Fig. 27. Two-point space-time correlation of axial velocity in the shear-layer at $r = 0.5D_j$, $x = 10.0D_j$. See also legend to Fig. 25.

Fig. 29. Predicted two-point correlation of axial velocity at three different locations in the shear-layer: '–○–' corresponds to a location $x = 2.5D_j$ downstream the nozzle exit, '–·–' to $x = 5.0D_j$ and '–∗–' to $x = 10D_j$. All points are located at $r = 0.5D_j$.

convective time scale in the current position in the flow. Comparing Figs. 25–27, the amplitude for a given spatial separation, ξ, increases downstream the jet, which indicates that the turbulence becomes more and more frozen in character, i.e. the turbulence length scale increases as the jet develops. A comparison was made with two-point measurements in the shear-layer at the end of the potential core, $x = L_c$. Here the potential core length is defined as the axial location where the centerline mean velocity equals $0.95U_j$. For the LES, this gives $L_c = 5.45D_j$ and, for the measured data, $L_c^{\text{exp}} = 6.50D_j$. For more detail on the two-point measurements see Jordan and Gervais (2003). In Fig. 28, correlation peak locations of the two-point space-time correlations obtained from LES data are compared with those from the two-point measurements. The agreement is, as can
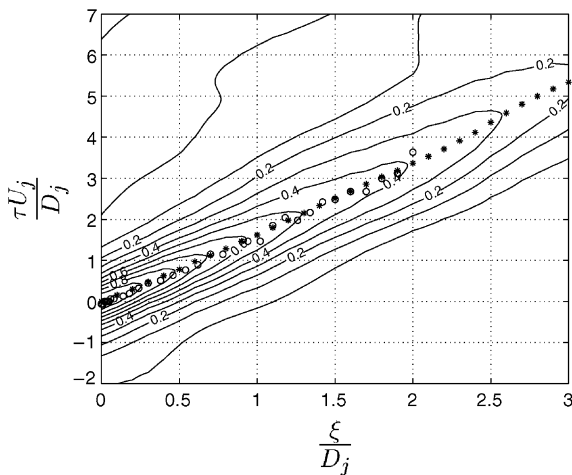
be seen, good. Fig. 29 shows predicted spatial correlations of axial velocity in three shear-layer locations. Here it can again be seen that the turbulence length scale increases downstream.

5.4. Turbulence length and time scales

Length and time scales of turbulence quantities have been obtained using the two-point space-time correlations presented in the previous section. Estimates of convection velocity of turbulence structures were also obtained for a number of axial locations in the shear-layer. The separation in time between the peak of the autocorrelation curve and the peak of the first following two-point space-time correlation curve was used. This time delay corresponds to a spatial separation of $0.1D_j$, as mentioned previously, and thus gives an estimate of the convection velocity, see Fig. 30. A more correct way would be not to use the temporal separation for the peak but rather the time for which the two-point space-time correlation envelope is a tangent to the correlation curve (Fisher and Davies, 1963). However, the result would not differ a great deal. Predicted convection velocities for a few axial locations are presented in Table 2. In the middle row, the convection velocities have been normalized by the jet velocity, U_j, and, in the right row, by the local mean velocity. As shown in Table 2, the eddy convection velocity is every where higher than the local mean velocity. This might be a nonintuitive result but is a phenomenon observed in experiments (Fisher and Davies, 1963; Wygnanski and Fiedler, 1969) and is caused by skewness of the velocity distribution. In shear-layer locations close to the high velocity potential core, the convection velocity is likely to be larger than the local mean velocity and lower in the outer parts of the shear-layer (Fisher and Davies, 1963).

Fig. 28. Contours of $\mathscr{R}_{uu}(\mathbf{x}, \xi, \tau)$ obtained in the shear-layer, $r = 0.5D_j$, at the end of the potential core, $x = L_c$. The contours corresponds to LES data, '∗' corresponds to the correlation peaks of these two-point space-time correlations and '○' to the peaks of the correlations at $x = L_c^{\text{exp}}$ obtained from the velocity data measured by Jordan and Gervais (2003).
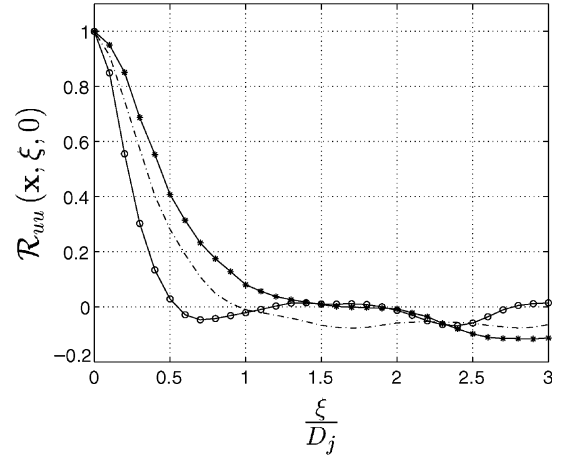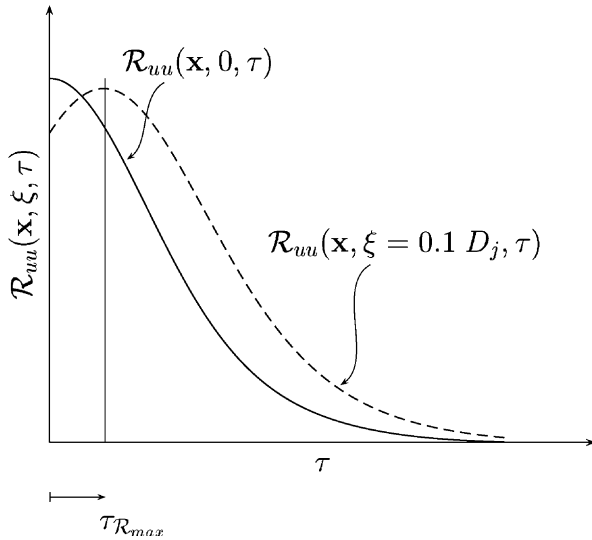
Fig. 30. The convection velocity of turbulence structures was estimated using the temporal separation, $\tau\mathscr{R}_{\max}$.

Local integral length and time-scales are estimated by integration of the corresponding autocorrelation and spatial correlation, respectively. The first crossing of the coordinate axis is used as the upper limit for the integration. The axial development of integral length and time scales are shown in Figs. 31 and 32. In these figures, scales obtained from measured data are represented by circles. The agreement between predictions and experiments is good.

5.5. Far-field sound pressure levels

Comparisons of predicted far-field sound pressure levels (SPL) and levels measured by Jordan et al. (2002b) are shown in Figs. 33 and 34. The time series of far-field pressure fluctuations used for the evaluation contains about 1.5×10^4 samples and is roughly 0.038 s. The observer locations for which sound pressure levels are presented in Fig. 33 are located on a $30D_j$ radius arc and those in Fig. 34 on a $50D_j$ radius arc. The observer locations in relation to the Kirchhoff surface used are shown in Fig. 1. The sound pressure level is here defined as

$$\text{SPL} = 20\log_{10}\left(\frac{(\langle(p')^2\rangle_t)^{0.5}}{p_{\text{ref}}}\right), \tag{17}$$

where

$$p_{\text{ref}} = (\rho_\infty c_\infty 10^{-12})^{0.5} = 2.0 \times 10^{-5} \; [\text{Pa}], \tag{18}$$
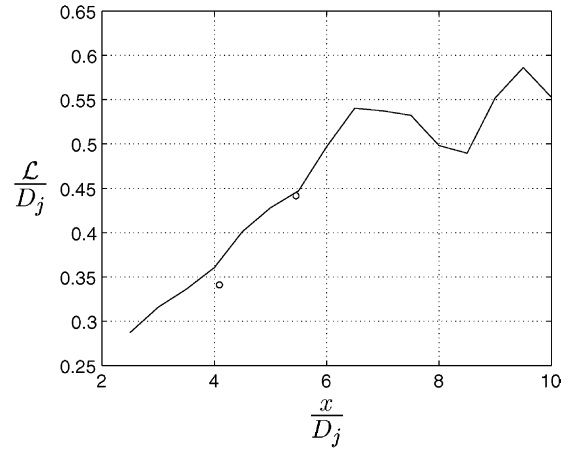

Fig. 31. Axial development of integral length scale in the shear-layer, i.e. $r = 0.5D_j$. '○' denotes experiments (Jordan and Gervais, 2003).
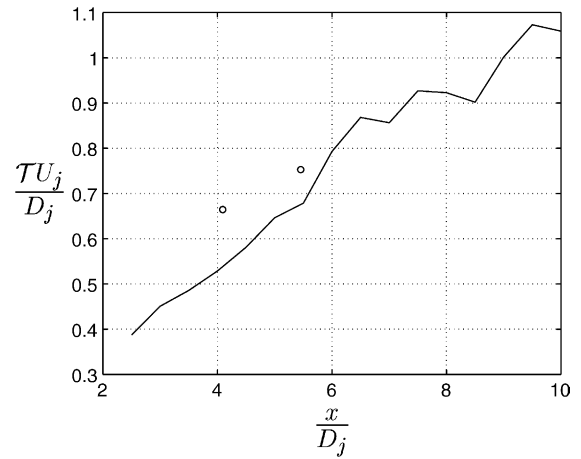

Fig. 32. Axial development of integral time scale in the shear-layer, i.e. $r = 0.5D_j$. '○' denotes experiments (Jordan and Gervais, 2003).

corresponds to the threshold of human hearing at a frequency of 1000 Hz. Sound pressure levels obtained using all spectral information available are often referred to as overall sound pressure levels (OASPL). The time history of pressure in the observer locations was obtained numerically using instantaneous flow data from the LES in combination with Kirchhoff surface integration. As can be seen in the figures, predicted levels agree very well with experimental data. The predicted sound pressure levels are for all observer locations within a 3 dB deviation from the measured levels and for most observer locations within a 1 dB deviation. The predicted lev-
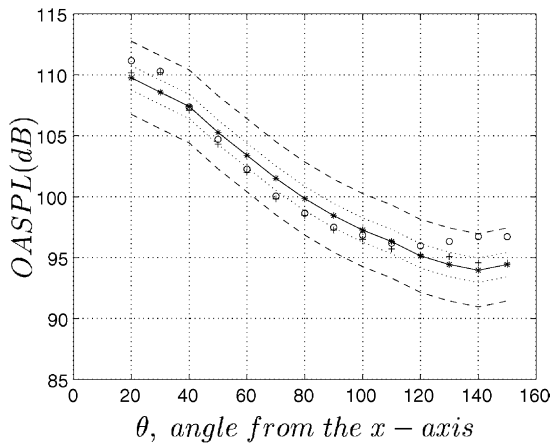
Table 2
Predicted convection velocity of turbulence structures in the shear-layer, $r = 0.5D_j$

x/D_j	3.00	4.00	5.00	6.00	7.00	8.00	9.00	10.00
u^c/U_j	0.71	0.71	0.65	0.60	0.71	0.65	0.65	0.56
$u^c/\langle u\rangle_t$	1.19	1.23	1.15	1.09	1.31	1.24	1.28	1.16

Fig. 33. Far-field sound pressure levels in microphone locations $30D_j$ from the nozzle exit: '–∗–' corresponds to sound pressure levels measured by Jordan et al. (2002b), the dashed lines to the measured levels ±3 dB and the dotted lines to the measured levels ±1 dB. '○' denotes predicted sound pressure levels using Kirchhoff surface integration and '+' SPL obtained using bandpass filtered pressure signals.

Fig. 34. Far-field sound pressure levels in microphone locations $50D_j$ from the nozzle exit. See also legend to Fig. 33.

els are not as good for angles below 40° and higher than 120° as for those in between. This is especially noticeable for the lower arc. In this case the fact that the observer locations are very close to the Kirchhoff surface might affect the levels obtained. Furthermore, removing the high frequency contribution and the contribution from very low frequencies by band-pass filtering the observer pressure signals significantly improves the results, see
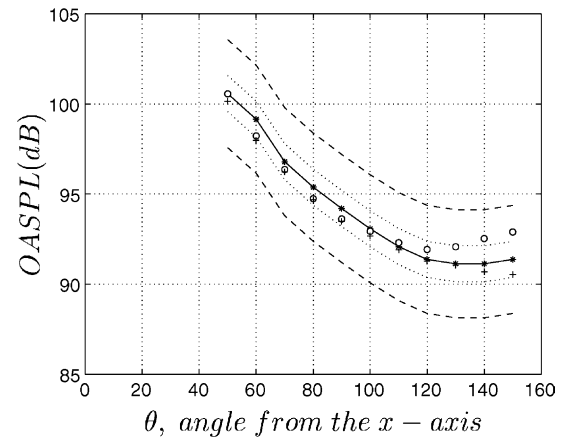
Figs. 33 and 34. The lower and upper cut-off frequencies of the band-pass filter used corresponds to $St = 0.05$ and $St = 1.0$, respectively. Fig. 35 shows a comparison of the power spectrum of predicted pressure fluctuations in a couple of observer locations with corresponding spectra obtained for the measured data (Jordan et al., 2002b). For low and high angles the predicted levels are in good agreement with the experimental data up to at least Strouhal number $St = 1.5$, see Fig. 35(a). For the intermediate angles on the other hand, the predicted amplitude decreases rapidly above $St = 1.0$. This is due to the fact that the grid is not fine enough to support high
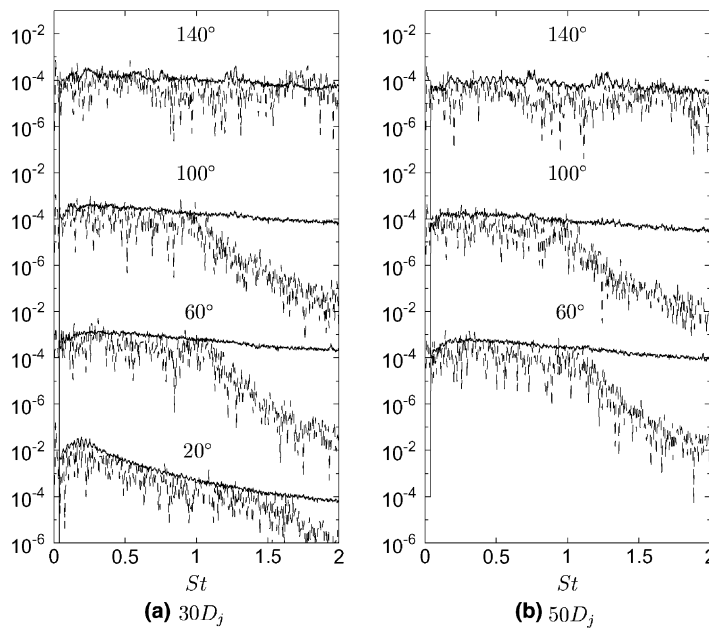

Fig. 35. Power spectrum of far-field pressure fluctuations versus Strouhal number, $St = fD_j/U_j$. The dashed line, '- - -' corresponds to predicted data obtained using Kirchhoff integration and the solid line corresponds to experimental data measured by Jordan et al. (2002b). In figure (a), four observer locations are represented. Starting at a location 20° from the x-axis, the angle is increased by an increment of 40° per spectrum. In figure (b) the first spectrum from below is obtained for an observer location 60° from the x-axis, i.e. it should be compared with the second spectra from below in figure (a). Note that the spectra have been staggered and the scale on the y-axis therefore is repeated.

frequency acoustic waves in the radial direction. Assuming that four cells per wavelength are required to be able to capture a propagating wave of a certain frequency, the cells in the area where the Kirchhoff surface is located would support propagating waves of Strouhal numbers up to $St \simeq 1.2$.

6. Concluding remarks

An LES of a compressible Mach 0.75 nozzle/jet configuration has been performed. The Reynolds number based on jet velocity and nozzle diameter was 5.0×10^4. Profiles of time and azimuthally averaged flow properties were compared with data measured by Jordan et al. (2002a). Although some deviations occur, the results are generally in good agreement with experiments. The good results are probably attributed to the homogeneity of the mesh used and the fact that a nozzle geometry has been included in the calculation domain. Using a combination of Cartesian and polar mesh blocks makes it possible to ensure that cells in the outer regions of the calculation domain are not too large and prevent cells from being clustered in the centerline region. The initial jet spreading and the potential core length are, however, not predicted correctly. Overpredicted $u'v'$ correlation close to the nozzle exit indicates that the degree of mixing is too high which makes the transition process too effective and hence the length of the potential region becomes shorter. This may be due to a combination of several factors such as: lack of subgrid scale dissipation, the numerical method used, entrainment boundary conditions and inflow conditions. Of these, the subgrid scale dissipation and the inflow conditions are believed to be the most important. Increasing the amount of subgrid scale dissipation would elongate the potential core region due to less effective mixing. Moreover, the initial mixing could probably be decreased by modification of the inflow conditions.

Two-point space-time correlations were obtained in a number of locations in the shear-layer along the nozzle lip-line. Correlation curves obtained at $x = L_c$ were in good agreement with experiments (Jordan and Gervais, 2003). Two-point space-time correlations in the shear-layer were used to obtain estimates of integral length scales, integral time scales and eddy convection velocities. The agreement with corresponding quantities obtained from the measured data was satisfying.

Sound pressure levels in the far-field were evaluated with a hybrid approach. Kirchhoff surface integration was utilized for propagation of sound to far-field locations. Instantaneous pressure on the Kirchhoff surface was obtained from the LES. Predicted sound pressure levels are in excellent agreement with measured levels (Jordan et al., 2002b). However, the mesh used fails to

capture waves of Strouhal numbers higher than $St \simeq 1.2$. This results in a rapid fall-off of the spectrum amplitudes for higher Strouhal numbers. The lower part of the spectra is accurately captured, however. Since the sound pressure levels obtained were in good agreement with the measured levels, capturing the lower part of the spectra seems to be sufficient to represent the main part of the radiated sound.

Appendix A. Convective flux scheme

The coefficients of low-dissipation upwind scheme used for estimation the convective flux over a cell face are derived using a third-order polynomial $Q(x)$ to represent the variation of the flow state in the direction normal to the face:

$$Q(x) = A + Bx + Cx^2 + Dx^3. \tag{A.1}$$

Assuming that the grid is equidistant, the cell averages of Q, represented by $\overline{Q}_1$ to $\overline{Q}_4$ in Fig. A.1, can be obtained by integrating $Q(x)$ over the cells as

$$\int_{-2}^{-1} Q(x)\,dx = A - \frac{3}{2}B + \frac{7}{3}C - \frac{15}{3}D = \overline{Q}_1,$$

$$\int_{-1}^{0} Q(x)\,dx = A - \frac{1}{2}B + \frac{1}{3}C - \frac{1}{4}D = \overline{Q}_2,$$

$$\int_{0}^{1} Q(x)\,dx = A + \frac{1}{2}B + \frac{1}{3}C + \frac{1}{4}D = \overline{Q}_3,$$

$$\int_{1}^{2} Q(x)\,dx = A + \frac{3}{2}B + \frac{7}{3}C + \frac{15}{4}D = \overline{Q}_4. \tag{A.2}$$

By rearranging the expressions in (A.2), the coefficients A, B, C and D can be expressed as functions of the state vectors $\overline{Q}_1$ to $\overline{Q}_4$:
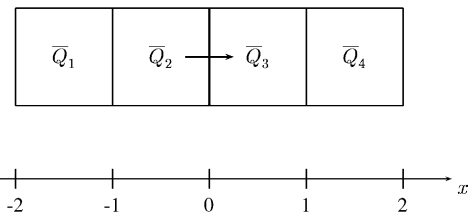

Fig. A.1. The face state is estimated using the state in four neighboring cells.

$$A = \frac{1}{12}\left[-\overline{Q}_1 + 7\overline{Q}_2 + 7\overline{Q}_3 - \overline{Q}_4\right],$$

$$B = \frac{1}{12}\left[\overline{Q}_1 - 15\overline{Q}_2 + 15\overline{Q}_3 - \overline{Q}_4\right],$$

$$C = \frac{1}{4}\left[\overline{Q}_1 - \overline{Q}_2 - \overline{Q}_3 + \overline{Q}_4\right],$$

$$D = \frac{1}{6}\left[-\overline{Q}_1 + 3\overline{Q}_2 - 3\overline{Q}_3 + \overline{Q}_4\right]. \tag{A.3}$$

The face state is evaluated using the interpolated value $Q(0)$, modified to include upwinding by adding the third derivative of $Q(x)$ according to

$$Q_0 = Q(0) + \delta Q'''(0) = A + 6\delta D$$
$$= C_1\overline{Q}_1 + C_2\overline{Q}_2 + C_3\overline{Q}_3 + C_4\overline{Q}_4, \tag{A.4}$$

where the coefficient, δ, in front of the upwind term has been chosen by numerical experiment (Mårtensson et al., 1991) to be $\frac{1}{96}$ in order to only introduce a small amount of upwinding. The result is the low-dissipation third-order upwind scheme used in this work:

$$\begin{cases} C_1 = -\left(\frac{1}{12} + \delta\right) = -\frac{9}{96}, \\[6pt] C_2 = \left(\frac{7}{12} + 3\delta\right) = \frac{59}{96}, \\[6pt] C_3 = \left(\frac{7}{12} - 3\delta\right) = \frac{53}{96}, \\[6pt] C_4 = \left(\frac{1}{12} - \delta\right) = -\frac{7}{96}. \end{cases} \tag{A.5}$$

A left hand side and right hand side version of Q_0 are obtained as

$$Q_L = C_1\overline{Q}_1 + C_2\overline{Q}_2 + C_3\overline{Q}_3 + C_4\overline{Q}_4,$$
$$Q_R = C_1\overline{Q}_4 + C_2\overline{Q}_3 + C_3\overline{Q}_2 + C_4\overline{Q}_1, \tag{A.6}$$

where subscripts L and R denotes left and right, respectively. The characteristic variables on the cell face are obtained using the estimates of the face state (A.6). Upwinded face states are then obtained using the characteristic variables. Whether the left hand side version or the right hand side version of Q should be used for calculation of the characteristic variables is determined by the signs of the characteristic speeds. The characteristic speeds are in turn obtained using a face state based on the average of $\overline{Q}_2$ and $\overline{Q}_3$.

References

Andersson, N., 2003. A study of Mach 0.75 jets and their radiated sound using large-eddy simulation. Licentiate thesis, Division of Thermo and Fluid Dynamics, Chalmers University of Technology, Gothenburg.

Billson, M., 2004. Computational techniques for turbulence generated noise. Ph.D. thesis, Division of Thermo and Fluid Dynamics, Chalmers University of Technology, Gothenburg.

Billson, M., Eriksson, L.-E., Davidson, L., 2002. Acoustic source terms for the linear Euler equations on conservative form. In: The 8th AIAA/CEAS Aeroacoustics Conference. No. 2582 in AIAA 2002. Breckenridge, CO.

Boersma, B., Brethouwer, G., Nieuwstadt, F., 1998. A numerical investigation on the effect of the inflow conditions on the self-similar region of a round jet. Physics of Fluids 10 (4), 899–909.

Bogey, C., Bailly, C., 2003. LES of a high Reynolds, high subsonic jet: effects of the inflow conditions on flow and noise. In: The 9th AIAA/CEAS Aeroacoustics Conference. No. 3170 in AIAA 2003. Hilton Head, SC.

Bogey, C., Bailly, C., Juvé, D., 2000a. Computation of the sound radiated by a 3-D jet using Large Eddy Simulation. In: The 6th AIAA/CEAS Aeroacoustics Conference. No. 2009 in AIAA 2000. Lahaina, HI.

Bogey, C., Bailly, C., Juvé, D., 2000b. Numerical simulation of sound generated by vortex pairing in a mixing layer. AIAA Journal 38 (12), 2210–2218.

Bogey, C., Bailly, C., Juvé, D., 2001. Noise computation using Lighthill's equation with inclusion of mean flow—acoustic interactions. In: The 7th AIAA/CEAS Aeroacoustics Conference. No. 2255 in AIAA 2001. Maastricht, Netherlands.

Bogey, C., Bailly, C., Juvé, D., 2003. Noise investigation of a high subsonic, moderate Reynolds number jet using a compressible large eddy simulation. Theoretical and Computational Fluid Dynamics 16 (4), 273–297.

Colonius, T., Lele, S., Moin, P., 1993. Boundary conditions for direct computation of aerodynamic sound generation. AIAA Journal 31 (9), 1574–1582.

Curle, N., 1955. The influence of solid boundaries on aerodynamic sound. Proceedings of the Royal Society A 231, 505–514.

DeBonis, J., 2004. A large-eddy simulation of a high Reynolds number Mach 0.9 jet. In: The 10th AIAA/CEAS Aeroacoustics Conference. No. 3025 in AIAA 2004. Manchester, United Kingdom.

DeBonis, J., Scott, J., 2002. A large-eddy simulation of a turbulent compressible round jet. AIAA Journal 40 (7), 1346–1354.

Eriksson, L.-E., 1995. Development and validation of highly modular flow solver versions in g2dflow and g3dflow. Internal report 9970-1162, Volvo Aero Corporation, Sweden.

Eriksson, L.-E., 2002. RANS prediction for test cases. Project deliverable D1.5, JEAN—EU 5th Framework Programme, G4RD-CT2000-00313, Volvo Aero Corporation, Sweden.

Erlebacher, G., Hussaini, M., Speziale, C., Zang, T., 1992. Toward the large-eddy simulation of compressible turbulent flows. Journal of Fluid Mechanics 238, 155–185.

Ffowcs Williams, J., Hawkings, D., 1969. Sound generated by turbulence and surfaces in arbitrary motion. Philosophical Transactions of the Royal Society, A 264, 321–342.

Fisher, M., Davies, P., 1963. Correlation measurements in a non-frozen pattern of turbulence. Journal of Fluid Mechanics 18, 97–116.

Freund, J., 2001. Noise sources in a low-Reynolds-number turbulent jet at Mach 0.9. Journal of Fluid Mechanics 438, 277–305.

Freund, J., Lele, S., Moin, P., 1996. Calculation of the radiated sound field using an open Kirchhoff surface. AIAA Journal 34 (5), 909–916.

Freund, J., Lele, S., Moin, P., 2000. Numerical simulation of a Mach 1.92 jet and its sound field. AIAA Journal 38 (11), 2023–2031.

Hussein, H., Capp, S., George, W., 1994. Velocity measurements in a high-Reynolds-number, momentum-conserving, axisymmetric, turbulent jet. Journal of Fluid Mechanics 258, 31–75.

Jordan, P., Gervais, Y., 2003. Modeling self and shear noise mechanisms in anisotropic turbulence. In: The 9th AIAA/CEAS Aeroacoustics Conference. No. 8743 in AIAA 2003. Hilton Head, SC.

Jordan, P., Gervais, Y., Valiére, J.-C., Foulon, H., 2002a. Final results from single point measurements. Project deliverable D3.4, JEAN—

EU 5th Framework Programme, G4RD-CT2000-00313, Laboratoire d'Etude Aeródynamiques, Poitiers.

Jordan, P., Gervais, Y., Valiére, J.-C., Foulon, H., 2002b. Results from acoustic field measurements. Project deliverable D3.6, JEAN—EU 5th Framework Programme, G4RD-CT2000-00313, Laboratoire d'Etude Aeródynamiques, Poitiers.

Le Ribault, C., Sarkar, S., Stanley, S., 1999. Large eddy simulation of a plane jet. Physics of Fluids 11 (10), 3069–3083.

Lyrintzis, A., 1994. Review: The use of Kirchhoff's method in computational aeroacoustics. ASME: Journal of Fluids Engineering 116, 665–676.

Mankbadi, R., 1999. Review of computational aeroacoustics in propulsion systems. Journal of Propulsion and Power 15 (4), 504–512.

Mankbadi, R., Shih, S., Hixon, R., Povinelli, L., 2000. Direct computation of jet noise produced by large-scale axisymmetric structures. Journal of Propulsion and Power 16 (2), 207–215.

Mårtensson, H., Eriksson, L.-E., Albråten, P., 1991. Numerical simulations of unsteady wakeflow. In: The 10th ISABE meeting, Nottingham, United Kingdom.

Mitchell, B., Lele, S., Moin, P., 1999. Direct computation of the sound generated by vortex pairing in an axisymmetric jet. Journal of Fluid Mechanics 383, 113–142.

Morris, P., Scheidegger, T., Long, L., 2000. Jet noise simulations for circular nozzles. In: The 6th AIAA/CEAS Aeroacoustics Conference. No. 2009 in AIAA 2000. Lahaina, HI.

Power, O., Kerhervé, R., Fitzpatrick, J., Jordan, P., 2004. Measurements of turbulence statistics in high subsonic jets. In: The 10th AIAA/CEAS Aeroacoustics Conference. No. 3021 in AIAA 2004. Manchester, United Kingdom.

Rembold, B., Adams, N., Kleiser, L., 2002. Direct numerical simulation of a transitional rectangular jet. International Journal of Heat and Fluid Flow 23 (5), 547–553.

Shur, M., Spalart, P., Strelets, M., Travin, A., 2003. Towards the prediction of noise from jet engines. International Journal of Heat and Fluid Flow 24 (4), 551–561.

Tucker, P., 2004. Novel MILES computations for jet flows and noise. International Journal of Heat and Fluid Flow 25 (4), 625–635.

Wollblad, C., Eriksson, L.-E., Davidson, L., 2004. Semi-implicit preconditioning for wall-bounded flow. In: The 34th AIAA Fluid Dynamics Conference and Exhibit. No. 2135 in AIAA 2004. Portland, OR.

Wygnanski, I., Fiedler, H., 1969. Some measurements in the self-preserving jet. Journal of Fluid Mechanics 38, 577–612.

Zhao, W., Frankel, S., Mongeau, L., 2001. Large eddy simulation of sound radiation from subsonic turbulent jets. AIAA Journal 39 (8), 1469–1477.